Evolution of the H-mode edge pedestal between ELMs

W. M. Stacey, Georgia Institute of Technology, Atlanta, GA 30332, USA
and
R. J. Groebner, General Atomics, San Diego, CA 92186, USA
August, 2010

Preprint of paper submitted to Phys. Plasmas

ABSTRACT The evolution of edge pedestal parameters between edge-localized modes (ELMs) is analyzed for an H-mode DIII-D [J Luxon, Nucl. Fusion 42, 612 (2002)] discharge. Experimental data are averaged over the same sub-intervals between successive ELMs to develop data that characterize the evolution of density, temperature, rotation velocities, etc. over the interval between ELMs. These data are interpreted within the context of the constraints imposed by particle, momentum and energy balance, in particular in terms of the pinch-diffusion relation for radial particle flux that is required by momentum balance. It is found that in the edge pedestal there is an increase of both inward (pinch) electromagnetic and outward (diffusive) pressure gradient forces over the inter-ELM interval.

I. INTRODUCTION

There is a longstanding interest (e.g. Refs. 1-4) in understanding the physics of the "pedestal" region in the edge of H-mode (high confinement mode) tokamak plasmas in which steep density and temperature gradients are observed to form. This interest stems at least in part from the observation (e.g. Refs. 5 and 6) that the "stiffness" observed in core temperature profiles implies that central temperatures achievable in future tokamaks (e.g. the International Thermonuclear Experimental Reactor--ITER) will depend on the values at the top of the edge pedestal.

The limiting values of pressure and pressure gradients that can be supported are generally understood to be set by the onset of MHD (magnetohydrodynamic) instabilities of the ballooning mode or kink (peeling) mode nature, in which large local bootstrap currents play a role (e.g. Ref. 7). However, an understanding of the physics processes determining the evolution of these steep density and temperature gradients prior to the onset of the limiting MHD instabilities and of the processes governing transport within the edge pedestal remains more elusive.

Detailed studies of the evolution of electron temperature and density profile evolution between ELMs in DIII-D[8,9] and ASDEX-U[10] give a general picture that pedestal profiles recover quickly after an ELM crash and then the rate of recovery slows markedly until the next ELM occurs. Fast (sub-millisecond) measurements of ion temperature and rotation in DIII-D have also shown a significant collapse and rapid rebuild at an ELM[11] (Edge-Localized Mode). However, studies in JT-60U have provided a somewhat different picture with the rate of recovery of Te and ne profiles being roughly constant between ELMs[12,13]. This difference in temporal behavior between JT-60U on one hand and DIII-D and ASDEX-U on the other hand is not understood.

An informal collaboration (the H-mode Edge Pedestal [HEP] Benchmarking Exercise[14]) has been formed among several theorists, modelers and members of the DIII-D experimental team to compare interpretations (using various codes) of experimental data from a single well-characterized DIII-D[15] H-mode edge pedestal (shot # 98889). Although the primary efforts of the group to date have concentrated on interpretation of energy transport in the edge pedestal, as summarized in Ref. 14, it has become clear that an interpretation of the density gradient data with a purely diffusive particle transport model would require an extremely small value of the diffusion coefficient ($D << 0.1\ m^2/s$) in the steep gradient region, suggesting the need to account for the presence of a particle pinch. There have been suggestions of a pinch since the earliest days of tokamak research on T3[16,17], continuing through ASDEX-U[18], JET[19,20], DIII-D[21], TCV[22]and Tore-Supra[23]. Analysis of the momentum balance equations has shown that the force balance among the pressure gradient and electromagnetic forces in fact requires that the radial particle flow in the edge plasma satisfies a "pinch-diffusion" relationship[24,25].

The temporal evolution of pedestal profiles is a tool that might provide insight into whether there is a particle pinch (more generally an inward force) in the pedestal. Indeed, time-dependent measurements in C-MOD[26] and ASDEX-U[27] show that transport of impurities has an inward pinch component, which can be reconciled with neoclassical theory. We are unaware of any measurements of

a particle pinch for the electrons or main ions in the pedestal. However, measurements in DIII-D[8], which show that the electron density barrier expands in time between ELMs, could be evidence of a pinch. Also, edge 2D modeling of JET discharges in a configuration optimized for edge diagnostics showed that either a pinch velocity or a spatially-varying diffusion coefficient is required to explain the observed density profiles and modeled particle source profiles[28].

In order to further test the pinch-diffusion relation for the radial particle flux, as well as to further elucidate the evolution of edge pedestal parameters, time-dependent edge pedestal data over the interval between ELMs (edge-localized modes), in which the steep gradients first collapse following an ELM and then build back up prior to the next ELM, have been prepared for this H-mode DIII-D shot that the HEP benchmarking collaboration is analyzing. The principal objective of this paper is to present an interpretation of the observed evolution of edge pedestal data based on the force balance (pinch-diffusion particle flux methodology[24, 25,29] previously developed for the interpretation of edge pedestal (non-MHD) phenomena. We note that we have previously examined[30] the evolution of the experimentally inferred thermal diffusivity between ELMs in this same DIII-D discharge

II. EXPERIMENTAL DATA

The lower single null, ELMing, H-mode discharge #98889 had parameters [I_p = 1.2 MA, B_ϕ =2.0 T, δ =0.07, P_{NB} = 3.1 MW, $n =$ 0.4x10^{20}/m^3] and an average ELM period of 36 ms over the time of interest, 3750-4110 ms into the discharge. The period between ELMs was separated into several time bins (e.g. the first 0-10% in the interval between one ELM and the next), and data in the same time bin for several successive inter-ELM intervals were combined and averaged in order to reduce random errors. A smooth fit to these data was then made to facilitate its analysis, particular the taking of derivatives to evaluate gradients. Both Thomson scattering and charge-exchange recombination (CER) measurements were used. Detailed discussions of these data preparation procedures and of the diagnostic measurements were given in Ref. 30 for the density and temperature data and in Ref. 29 for the rotation and radial electric field data.

The fits to the measured data for the electron density for three different inter-ELM time bins are plotted in Fig. 1, and the fits to the measured temperatures are plotted in Figs. 2 and 3. The time bin 0-10% is immediately after the ELM crash, the time bin 40-60% is in the middle of the interval between ELMs, and the time bin 80-99% is immediately before the following ELM. The sharp pedestals that obtained just before the ELM crash (80-99%) are evident when compared with the reduced gradients in the profiles immediately after the ELM crash (0-10%) in Figs. 1 and 2 for the electron density and temperature, which were made with Thomson scattering measurements with a very high time resolution (<< 1 ms)with respect to the span of the time bins. The recovery of the density and temperature pedestal profiles occur very quickly after the ELM crash, as indicated by the similarity of the profiles for the 40-60% and 80-99% time bins.

The fits to the measured CER ion temperature data in Fig. 3 do not reflect an ion temperature profile collapse immediately following the ELM, but this is believed to be an artifact of the 10 ms

integration time of the CER data used in this shot, which is about 3 times longer than the 0-10% time bin in this shot. The CER system is capable of making measurements with sub-millisecond integration times, although this mode of operation is rarely used because the signal to noise decreases as the integration time decreases and the temporal coverage of the plasma is reduced due to the available memory for the digitized data. However, measurements with integration times of 0.55 ms or less in other shots have clearly shown substantial drops in pedestal profiles for Ti for C6+ ions[11,30, 31]. CER measurements with a time resolution of 5 ms have also shown a drop in Ti at an ELM crash[32] for a discharge with an average ELM period of 60 ms. In this dataset, the changes were less marked than observed for data obtained with sub-millisecond integration times, possibly because of temporal evolution over the dynamics of the Ti profile. Thus, for discharge 98889 under discussion here, it is very plausible that the Ti (and rotation) profiles changed significantly immediately following the ELM crash but these effects were not resolved because the CER measurements were averaged over about one-third of the ELM period.

Fits of the measured CER carbon rotation data and the radial electric field constructed from the data and the measured carbon pressure gradient (using the toroidal momentum balance for carbon) are shown in Figs. 4-6. The comments made above about the time resolution of the CER data apply also to Figs. 4-6. In other shots with shorter integration times, marked drops were observed in the C6+ pedestal profiles for the toroidal velocity[11,31] , and significant changes were observed in the poloidal velocity profile[11] at an ELM crash. The larger rotation velocities shown for the 40-60% time bins in Figs. 4 and 5 may be due to the fact that none of the data points in this bin included the ELM crash. Similarly, the more fully formed electric field well for the 40-60% time bin in Fig. 6 also may be due to the fact that none of the data in that time bin included the ELM crash.

The temporal averaging of the Thomson scattering data (<< 1 ms) is more than adequate to characterize the time evolution of electron density and temperature over the inter-ELM interval. These time resolution considerations will be important in interpreting the CER data for the 0-10% bin in the following sections.

III. PLASMA FLUID EQUATIONS

Interpretation of the data presented in Figs. 1-6 will be based on the use of that data to evaluate the physical constraints imposed by particle, momentum and energy balance, as represented by the plasma multi-fluid equations. The main plasma ions satisfy the continuity equation

$$\frac{\partial \Gamma_i}{\partial r} = -\frac{\partial n_i}{\partial t} + n_e n_o \left\langle \sigma \upsilon \right\rangle_{ion} + S_{nb} \qquad (1)$$

where $\Gamma_i = n_i V_{ri}$ is the radial ion particle flux. The second term on the right represents the electron ionization of recycling neutral atoms of the main plasma species, and the third term represents the source of plasma ions due to neutral beam injection.

All ion species (and the electrons) satisfy a momentum balance equation, the toroidal, radial and poloidal components of which can be represented, respectively, by

$$n_j m_j [(\nu_{jk} + \nu_{dj}) V_{\phi j} - \nu_{jk} V_{\phi k}] = n_j e_j E_\phi^A + n_j e_j B_\theta V_{rj} + M_{\phi j} \quad (2)$$

$$V_{\phi j} = \frac{1}{B_\theta}\left[E_r + V_{\theta j} B_\phi - \frac{1}{n_j e_j}\frac{\partial p_j}{\partial r} \right] \quad (3)$$

and

$$\left[\frac{q\upsilon_{thj} f_j}{R} + \nu_{jk} + \nu_{atomj} \right] V_{\theta j} - \nu_{jk} V_{\theta k} = -\frac{e_j V_{rj} B_\phi}{m} + \frac{\upsilon_{thj} f_j q}{R}\left[\frac{B_\phi K^j T_j L_{Tj}^{-1}}{e_j B^2} + \frac{\upsilon_{thj} E_r}{B_\theta} \right] \quad (4)$$

The quantity ν_{dj} is a toroidal angular momentum transfer frequency which represents the combined effect of viscosity, inertia, atomic physics, and other "anomalous" processes. Justification of representing the toroidal momentum transfer processes in this form is discussed in Ref. 33, and the derivation of Eq. (4) is given in Ref. 34. The value of this momentum transfer frequency will be determined from the experimental data. The quantity K^j is a ratio of Hirshman-Sigmar coefficients given in Ref. 34, and $f_j = \varepsilon^{-3/2}\nu_{jj}^* \Big/ \left[\left(1 + \varepsilon^{-3/2}\nu_{jj}^*\right)\left(1 + \nu_{jj}^*\right) \right]$ arises from the use of the parallel viscosity coefficient $\eta_{oj} = n_j m_j \upsilon_{thj} q R f_j$. $M_{\phi j}$ is the toroidal angular momentum input (e.g. by neutral beams). ν_{jk} is the interspecies collision frequency, and ν_{atomj} represents the charge-exchange and elastic scattering collision frequency for the ion species j with neutral atoms. When more than two ion species are present, the terms with a *k* subscript in the momentum balance equations for ion species *j* are understood to be summed over the other *k* ion species. (Momentum time derivative terms are suppressed above because the CER data are not sufficiently well resolved to evaluate the rate of change of rotation velocities. This is probably not an issue for the toroidal velocity terms, which make a small contribution to the pinch velocity in any case. It may introduce an additional uncertainty into the poloidal velocity contribution to the pinch velocity, but this uncertainty is small compared to the uncertainty already present because of the unavailability of measured deuterium poloidal velocities.)

Heat balance equations for the electrons

$$\frac{\partial Q_e}{\partial r} = -\frac{\partial}{\partial t}\left(\frac{3}{2} n_e T_e \right) + q_{nbe} + q_{ie} - n_e n_o \langle \sigma\upsilon \rangle_{ion} E_{ion} - n_e n_z L_z \quad (5)$$

and for the ions summed over species

$$\frac{\partial Q_i}{\partial r} = -\frac{\partial}{\partial t}\left(\frac{3}{2} n_i T_i \right) + q_{nbi} - q_{ie} - n_e n_o^c \langle \sigma\upsilon \rangle_{cx} \frac{3}{2}\left(T_i - T_o^c \right) \quad (6)$$

determine the radial distribution of the of the total heat fluxes of electrons and ions across the edge pedestal. Here, q_{nb} is the neutral beam (or other external) heating source rate, q_{ie} is the collisional heat exchange from ions to electrons, E_{ion} is the ionization potential, L_z is the radiation emissivity rate of the impurity species *z*, the subscript *cx* refers to charge-exchange plus elastic scattering, and the superscript *c* denotes the *cold* neutral atom species that have penetrated into the pedestal but not yet collided.

IV. ION PARTICLE FLUX

In order to solve Eq. (1) over the edge pedestal region to determine the ion particle flux, it is also necessary to calculate the recycling neutral flux into the edge plasma. In order to do this we perform a global particle balance on the entire plasma to determine the ion particle flux crossing the separatrix into the scrape-off layer (SOL), which can then be used as a boundary condition for Eq. (1). This iterative calculation performed by the GTEDGE code[20] involves a core particle balance with neutral beam and recycling neutral sources to determine the ion flux into the SOL, a 2-point divertor model calculation with this input particle flux to determine the ion flux to the divertor plate and the recycling neutral flux, and a two-dimensional transport calculation of the neutral atoms through the divertor region to fuel the plasma. This calculation is adjusted to match certain experimental data; the neutral recycling source is adjusted so that the core particle balance calculation yields the measured line-average electron density, the measured energy and particle confinement times and the measured radiation are used in the global particle and power balances to determine heat and particle fluxes from the core into the scrape-off layer, geometric model parameters are adjusted to calculate the measured density and temperature at the outer mid-plane separatrix and at the divertor plate (if available). Because we are unable to calculate a time-dependent neutral ionization source over the inter-ELM interval, we calculate a single ionization source distribution for plasma properties averaged over the inter-ELM interval and use it for calculating the ion distribution for all three time bins.

The deuterium ion particle flux in the edge calculated in this manner from Eq. (1) is shown in Fig. 7 for the three different time bins in the inter-ELM interval. The ion particle flux is inward (negative) over much of the edge immediately after the ELM crash (0-10%), but recovers quickly and becomes outward over most of the time interval between ELMs. Only the experimental electron density and temperature are used in solving Eq. (1), and since these quantities are based on Thomson scattering measurements, the results shown in Fig. 7 are in fact reflective of the evolution of the ion particle fluxes over the inter-ELM interval. It is important to note that experimental values of the local density time derivatives were used in determining these results.

V. MOMENTUM TRANSPORT AND PARTICLE PINCH

The radial and toroidal momentum balance Eqs. (2) and (3) may be combined to define a force balance constraint that must be satisfied by the radial ion particle flux[24,25]

$$\Gamma_j \equiv n_j V_{rj} = \frac{n_j m_j \left(\nu_{jk} + \nu_{dj}\right) T_j}{\left(e_j B_\theta\right)^2} \left[\left(\frac{1}{p_j} \frac{\partial p_j}{\partial r} \right) - \frac{e_j}{e_k} \frac{\nu_{jk}}{\left(\nu_{jk} + \nu_{dj}\right)} \left(\frac{1}{p_k} \frac{\partial p_k}{\partial r} \right) \right] + n_j V_{rj}^{pinch} \qquad (7)$$

where the normalized collection of force terms other than those associated with the pressure gradient

$$V_{rj}^{pinch} \equiv \frac{\left[-M_{\phi j} - n_j e_j E_\phi^A + n_j m_j \left(\nu_{jk} + \nu_{dj}\right) \left(f_p^{-1} V_{\theta j} + E_r / B_\theta \right) - n_j m_j \nu_{jk} V_{\phi k} \right]}{n_j e_j B_\theta} \qquad (8)$$

is identified as a "velocity pinch".

For the main ion species $e_j/e_k << 1$, so that with the approximation that the impurity logarithmic pressure gradient is the same as for the main ions, Eq. (7) can be written as a pinch-diffusion relation for the main ion radial particle flux

$$\Gamma_j = -\frac{n_j D_j}{p_j} \frac{\partial p_j}{\partial r} + n_j V_{rj}^{pinch} = -D_j \left(\frac{\partial n_j}{\partial r} + \frac{n_j}{T_j} \frac{\partial T_j}{\partial r} \right) + n_j V_{rj}^{pinch} \qquad (9)$$

where the diffusion coefficient is

$$D_j \equiv \frac{m_j T_j \nu_{jk}}{\left(e_j B_\theta\right)^2} \left(1 + \frac{\nu_{dj}}{\nu_{jk}} - \frac{e_j}{e_k} \right) \qquad (10)$$

For a typical DIII-D plasma with deuterium main ion species and a dominant carbon impurity species, all of the quantities on the right side of Eq. (8), except the deuterium (j) poloidal rotation, can be determined experimentally. The external momentum input, which is a small term in Eq. (8) in the edge, can be calculated from the known beam geometry and power input. The induced toroidal electric field, which is also a small term, can be determined from the measured loop voltage. The density, temperature, radial electric field and carbon (*k*) toroidal rotation velocity are measured, and ν_{jk} can be calculated using the measured density and temperature.

The momentum transfer frequencies for deuterium (ν_{dj}) and carbon (ν_{dk}) can also be inferred from experimental data by solving the coupled toroidal momentum balance Eqs.(2) for the two species "backwards", using the measured rotation velocities as known inputs, to obtain[24,25]

$$\nu_{dj} = \nu_{jk} \left[\frac{n_j e_j E_\phi^A + e_j B_\theta \Gamma_j + M_{\phi j}}{n_j m_j \nu_{jk} V_{\phi j}} - \left(1 - \frac{V_{\phi k}}{V_{\phi j}} \right) \right] \qquad (11)$$

and a similar equation with the *j* and *k* subscripts interchanged. Since the deuterium rotation velocities are not measured, we make use of a perturbation analysis[24,25] in which $\left(V_{\phi j} - V_{\phi k}\right)$ is taken as a small

parameter to derive expressions which may be used to evaluate the experimental deuterium (*j*) and carbon (*k*) toroidal angular momentum transfer frequencies for the main ions

$$\nu_{dj} = \frac{\left(n_j e_j E_\phi^A + e_j B_\theta \Gamma_j + M_{\phi j}\right) + \left(n_k e_k E_\phi^A + e_k B_\theta \Gamma_k + M_{\phi k}\right)}{\left(n_j m_j + n_k m_k\right) V_{\phi k}^{\exp}} \tag{12}$$

and for the carbon impurity ion

$$\nu_{dk} = \frac{\left(n_k e_k E_\phi^A + e_k B_\theta \Gamma_k + M_{\phi k}\right) + n_j m_j \nu_{jk} (V_{\phi j} - V_{\phi k})_0}{n_k m_k V_{\phi k}^{\exp}} \tag{13}$$

where

$$(V_{\phi j} - V_{\phi k})_0 = \frac{\left(n_j e_j E_\phi^A + e_j B_\theta \Gamma_j + M_{\phi j}\right) - n_j m_j \nu_{dj} V_{\phi k}^{\exp}}{n_j m_j \left(\nu_{jk} + \nu_{dj}\right)} \tag{14}$$

is the first order perturbation estimate of the difference in deuterium and carbon toroidal rotation velocities. Evaluation of Eq. (14) using the data for shot 98889 reveals that this difference is in fact small compared to the measured carbon rotation for the discharge being considered, confirming the validity of the perturbation analysis.

The deuterium toroidal angular momentum transfer frequency determined by using the measured data to evaluate Eq. (12) is shown in Fig. 8. Over most of the inter-ELM interval this momentum transfer is outward (positive transfer frequency) and increases sharply just inside the separatrix. Note that this momentum transfer frequency inferred from experimental data is due to a variety of physical mechanisms, known and unknown. The charge exchange momentum transfer frequency was calculated to be significantly smaller than the values shown in Fig. 8, confirming that other physical mechanisms are involved.

Immediately after the ELM crash (0-10%) the inferred momentum transfer frequency is negative, implying inward transfer. A similar result was found for the carbon momentum transfer frequency. This negative momentum transfer frequency may be an artifact of the inadequate resolution in the CER rotation measurements. The ion particle flux used to evaluate Eq. (12) is inward (Fig. 7) for the 0-10% time bin, and the Thomson data used in determining the particle flux are adequately resolved. On the other hand, the CER data used to determine the carbon toroidal rotation velocity involves measurements averaged over about one-third of the inter-ELM interval. Note that the CER toroidal rotation data in Fig. 4 do not reflect a crash immediately after an ELM, as found in Ref. 11, in which the CER data were better resolved. Furthermore, the better resolved Thomson scattering data used to evaluate Eq. (1) shows very different particle fluxes immediately after the ELM crash. Thus, the inference of inward angular momentum transport (negative momentum transfer frequency) immediately following an ELM is at least questionable.

The evaluation of the deuterium pinch velocity by using measured data to evaluate Eq. (8) is straightforward except for the determination of the deuterium poloidal rotation velocity appearing in that expression. We can calculate this velocity using Eq. (4) and have done this two ways for time bin 40-60%, which should be least affected by data from the ELM crash. First, we solved the coupled pair of Eqs. (4) for both the carbon and deuterium velocities; the results are plotted as V_C^{calc} and V_D^{calc1} in Fig. 9. The second calculation used the experimental carbon velocity in Eq. (4) to calculate the deuterium velocity, which result is plotted as V_D^{calc2} in Fig. 9. There is virtually no difference in the two calculated deuterium rotation velocities (which fall on the same plot in Fig. 9), but there is a significant difference between the calculated deuterium velocity and both the calculated and measured carbon velocities, which discourages the use of a perturbation analysis, as was done for the toroidal velocity. There also is a significant difference between the calculated and measured carbon velocities, which indicates that there is some edge physics (e.g. ion orbit loss) missing in Eq. (4) in the sharp gradient region. (Note that the agreement between the calculated and measured poloidal rotation for carbon is quite good in the flattop region rho < 0.95.)

In order to accommodate both the experimental evidence that something is missing from the calculation model and the calculation evidence that there is a difference in the deuterium and carbon velocities, we use the difference between the calculated and measured carbon velocities to correct the calculated deuterium poloidal velocity at each radius. This corrected deuterium poloidal velocity, plotted as V_D^{cor} in Fig. 9 and in Fig. 10, is used as a surrogate for the deuterium poloidal velocity in evaluating the pinch velocity. This uncertainty in the deuterium poloidal velocity determination introduces an estimated uncertainty of about 30-40% into the calculation of the pinch velocity.

The experimental pinch velocities, evaluated using the measured carbon toroidal rotation velocities and radial electric fields and the "corrected" deuterium poloidal rotation velocities, are plotted for the three time bins in Fig. 11. The inward particle pinch velocity is large in the steep gradient region midway between ELMs (40-60%) and becomes larger just before the ELM crash (80-99%). Then, immediately following the ELM crash (0-10%), the pinch velocity becomes outward in the steep gradient region. Another way to put this is that the net electromagnetic force on the ions is strongly inward immediately before the ELM crash and becomes outward immediately after the ELM crash. The increase in the deuterium poloidal velocity (i.e. in the $V_\theta \times B_\phi$ radial force) from just after the ELM crash (0-10%) to just before the next ELM (80-99%) shown in Fig. (10) is the dominant cause for the increase in pinch velocity in the steep gradient region calculated from Eq. (5) in this shot. We note that the 10ms resolution of the CER data (rotation velocities, ion temperature, Er) introduces uncertainty in the "outward pinch" inferred for the 0-10% bin immediately after the ELM crash.

The evolution of the experimentally inferred diffusion coefficients, obtained by using measured data to evaluate Eq. (10), is plotted in Fig. 12. (Note that the evaluation of D does not depend on either the poloidal velocity or the pinch velocity.) Midway between ELMs, D increases radially from < 0.5 m^2/s in the flattop region to > 1 m^2/s just inside the separatrix. Just before the ELM crash (80-99%), D increases to > 4 m^2/s just inside the separatrix. At the same time, the inward pinch velocity in the sharp gradient region increases (becomes more negative) from (40-60%) to (80-99 (Fig. 11). The implication is that there are evolutions of large inward electromagnetic forces and slightly larger outward pressure

gradient forces which result in the evolution of the net outward particle fluxes shown in Fig. 7. Immediately after the ELM crash (0-10%), the diffusion coefficient becomes negative, which is an unphysical artifact of the insufficient resolution of the CER data in this time bin.

VI. ENERGY TRANSPORT

The heat conduction relation $q = -n\chi\,\partial T/\partial r$ can be used to interpret the measured temperature and density profiles in terms of the inferred experimental value of the thermal diffusivity

$$\chi_{i,e}^{\exp} = L_{Ti,e}^{\exp}\frac{q_{i,e}}{n_{i,e}^{\exp}T_{i,e}^{\exp}} = \frac{L_{Ti,e}^{\exp}}{n_{i,e}^{\exp}T_{i,e}^{\exp}}\left[Q_{i,e} - \frac{5}{2}T_{i,e}^{\exp}\Gamma_{i,e}\right] \tag{15}$$

where $L_T^{-1} = (1/T)(\partial T/\partial r)$.

The total heat and particle fluxes are determined by solving Eqs. (1), (5) and (6) in the edge pedestal. As discussed above for the particle flux, boundary conditions on these equations are obtained from iterating a global particle and energy balance on the core plasma, a 2-point divertor calculation of the ion flux to the divertor target, and a two-dimensional calculation of the recycling neutral particle transport[35]. Measured radiation power loss from the core and divertor and energy confinement times are used in the global energy balance. This balance yields the total heat flux crossing the separatrix, but not the split between the electron and ion heat fluxes. A one-dimensional transport calculation with the ONETWO code[36] of the core plasma yielded a 3/1 electron/ion split, which was used in these calculations.

The total electron and ion heat fluxes calculated from Eqs. (5) and (6), using the measured temperatures and densities of Figs. 1-3, are plotted in Fig. 13 for the different inter-ELM time bins. The time derivative terms in these equations [and in Eq. (1) for the particle flux] were also evaluated using experimental data; the rapid cooling of the edge pedestal is the cause of the radially increasing heat flux just before (80-99%) the ELM crash. While the evaluation of the particle flux and the electron heat flux are not directly affected by the lack of resolution in the CER data, an inward (negative) ion heat flux calculated for the 1-10% time bin (not shown) may be an artifact of using too large a value of ion temperature that does not reflect the expected reduction in this quantity following the ELM crash.

The electron and ion experimental thermal diffusivities determined by using the conductive heat fluxes of Fig. 13 in Eq. 15 are plotted in Figs. 14 and 15, respectively. The electron thermal diffusivity is larger by a factor of 2 in the steep gradient region, and lower by 20% in the flattop region, just after the ELM crash (0-10%) than just before it (80-99%). The inferred ion thermal diffusivity in the steep gradient region increases over the inter-ELM time interval. However, the methodology breaks down for the time immediately after the ELM crash (0-10%) when unphysical negative values of the ion thermal diffusivity are calculated due to the 10 ms resolution of the CER ion temperature measurements. These results are consistent with those reported[30] previously for this discharge, but with quantitative differences due to the use of improved data fits, of fits to the time derivatives, of using the 75/25 (rather than 50/50) electron/ion heat split at the separatrix, etc.

VII. CONSISTENCY

Equation (9) can be rearranged to obtain an expression for the ion pressure gradient

$$-\frac{1}{p_j}\frac{\partial p_j}{\partial r} = \frac{V_{rj} - V_{rj}^{pinch}}{D_j} \qquad (16)$$

that can be integrated to calculate the ion density ($n_j = p_j / T_j$) distribution in the plasma edge. The measured rotation velocities and radial electric field largely determine V_{rj}^{pinch} , and the neutral beam and recycling neutral sources determine V_{rj} via the continuity equation. The electron density profile calculated from the integration of Eq. (16) (and a carbon density correction) is compared with the profile measured with Thomson scattering in Fig. 15. The agreement is quite good in the steep gradient region for the 80-90% time bin (and for the 40-60% time bin not shown), where the effects of the ELM crash should be minimal. The agreement is somewhat poorer in the 0-10% time bin, where the lack of resolution in the CER data introduces more of an inconsistency. The poorer agreement in profile shape in the flattop region is attributed to the approximate treatment of the deuterium poloidal velocity, to the use of a slab geometry approximation in integrating the equations inward from the separatrix, and to an approximate analytical calculation of beam deposition profile in the edge, which starts to affect the calculation inside of rho = 0.95.

VIII. SUMMARY AND CONCLUSIONS

In order to provide insight about the evolution of plasma parameters in the H-mode edge pedestal, time dependent data were developed over different time bins in the inter-ELM intervals of average value 36 ms in a representative DIII-D discharge. These data have been used to evaluate the constraints imposed by the particle, momentum and energy balances. Within the limits of the time resolution of the CER experimental data, the measurements can be consistently reconciled by the force-balance analysis leading to a pinch-diffusion constraint on the radial particle flux that is required by momentum balance. The evolution of particle, angular momentum and heat transport coefficients were inferred from the experimental data.

Evaluation of the pinch-diffusion relation for the radial particle flux imposed by momentum constraints indicates that the net radial particle flux in the edge pedestal is determined by a near balance between a large inward electromagnetic force (the pinch-- produced primarily by rotation and the radial electric field) and a large outward diffusive force (produced by the pressure gradient). Both of these forces increase with time between ELMs in the sharp-gradient edge pedestal region, although the data were not sufficiently resolved in time to determine unambiguously what took place

immediately following an ELM crash. The increase in time of the pinch velocity between ELMs was due primarily to the increasing deuterium poloidal rotation velocity and radial $V_\theta \times B_\phi$ force.

Determination of the deuterium poloidal velocity is probably the major uncertainty in the interpretation of the pinch velocity from experimental data. Techniques to measure this quantity would be a valuable addition to the diagnostic set. Meanwhile, an experiment with a main plasma ion whose rotation velocity can be measured (e.g. helium) could be performed. The theory for poloidal rotation in the plasma edge does not satisfactorily agree with the measured carbon rotation velocities in the sharp gradient region. Improvement in this theory is needed to advance interpretation of edge pedestal data such as presented in this paper, and for other reasons.

ACKNOWLEDGEMENT

This work was supported by the U. S. Department of Energy Grant No. DE-FG01-ER54538 with the Georgia Tech Research Corporation and by the U. S. Department of Energy Contract N. DE-AC03-99ER54463. The authors are grateful to other members of the DIII-D Team who took part in measuring and analyzing the data used in this paper. The first author appreciates the hospitality provided by General Atomics during part of this work.

References

1. A. E. Hubbard, R. L. Boivin, R. S. Granetz,xxxx, Phys. Plasmas 5, 1744 (1998).
2. R. J. Groebner and T. H. Osborne, Phys. Plasmas 5, 1800 (1998).
3. W. Suttrop, O. Gruber, B. Kurzan xxx, Plasma Phys. Controlled Fusion 42, A175 (2000).
4. E. Hubbard, Plasma Phys. Controlled Fusion 42, A15 (2000).
5. M. Kotschenreuther, W. Dorland, Q. P. Liu xxxx, Proceedings of the 16th Conference on Plasma Physics and Controlled Fusion Research, Montreal 1996 (IAEA, Vienna, 1997), Vol. 2, p371.
6. J. E. Kinsey, G. Bateman, T. Onjun, A. H. Kritz, A. Pankin, G. M. Staebler and R. E. Waltz, Nucl. Fusion 43, 1845 (2003).
7. P. B. Snyder, H. R. Wilson, J. R. Ferron, L. L. Lao, A. W. Leonard, T. H. Osborne, A. D. Turnbull, D. Mossessian, M. Murikami and X. Q. Xu, Phys. Plasmas 9, 2037 (2002).
8. R. J. Groebner, A. W. Leonard, P. B. Snyder, T. O. Osborne, C. F. Maggi, M. E. Fenstermacher, C. C. Petty, and L. W. Owen, *Nucl. Fusion* 49, 085037 (2009).
9. R.J. Groebner , P.B. Snyder, T.H. Osborne , A.W. Leonard , T.L. Rhodes, L. Zeng , E.A. Unterberg , Z. Yan , G.R. McKee, C.J. Lasnier, J.A. Boedo and J.G. Watkins, Nucl. Fusion **50,** 064002 (2010).
10. E.Wolfrum, A. Burckhart, R. Fischer, N. Hicks, C. Konz, B. Kurzan, B. Langer, T. Putterich, H. Zohm and the ASDEX Upgrade Team *Plasma Phys. Control. Fusion* **51,** 124057 (2009).
11. M. R.Wade, K. H. Burrel, J. T. Hogan, A. W. Leonard, T. H. Osborne, P. B. Snyder and D. Coster, *Phys. Plasmas* **12,** 056120 (2005),
12. M.Yoshida, *et al., Plasma Phys. Control. Fusion* **48,** A209 (2006).
13. N. Oyama, Journal of Physics: Conference Series **123,** 012002 (2008).
14. J. D. Callen, R. J. Groebner, T. H. Osborne, J. M. Canik, L. W. Owen, A. Y. Pankin, T. Rafiq, T. D. Rognlien and W. M. Stacey, Nucl. Fusion 50, 064004 (2010).
15. J. Luxon, Nucl. Fusion 42, 614 (2002).
16. L. A. Artsimovich, Plasma Phys. Controlled Nucl. Fusion Research 2, 595 (1966).
17. E. P. Gorbunov, Plasma Phys. Controlled Nucl. Fusion Research 2, 629 (1966).
18. J. Stober, C. Fuchs, O. Gruber, M. Kaufmann, B. Kurzan, F. Meo, H. W. Muller, F. Ryter and ASDEX-U team, Nucl. Fusion 41, 1535 (2001).
19. M. Valovic, J. Rapp, J. G. Cordey, R. Budney, D. C. McDonald, L. Garzotti, A. Kallenback, M. A. Mahdavi, J. Ongena, Va. Parail, G. Saibene, R. Sartori, M. Stamp, O. Sauter, J. Strachan, W. Suttrop and EFDA_JET team, Plasma Phys. Controlled Fussion 44, 1911 (2002).
20. L. Garzottie, 29the EPS Conference on Plasma Physics and Controlled Fusion, Montreux, 2002 (Institute of Physics, University of Reading, Berkshire, 2002), Vol. 26B, p 1035.
21. D. R. Baker, M. R. Wade, C. C. Petty, M. N. Rosenbluth, T. C. Luce, J. S. deGrassie, B. W. Rice, R. J. Groebner, C. M. Greenfield, E. J. Doyle, C. L. Rettig, T. L. Rhodes and M. A. Mahdavi, Nucl. Fusion 40, 1003 (2000).
22. H. Weisen and E. Minardi, Europhys. Lett. 56, 542 (2001).

23. G. T. Hoang, C. Bourdelle, B. Pegourie, B. Schunke, J. F. Artaud, J. Bucalossi, F. Clairet, C. Fonzi-Bonizec, X. Garbet, C. Gill, R. Guirlet, F. Imbeaux, J. Lasalle, T. Loarer, C. Lowry, J. M. Travere, E. Tsitrone and Tore Supra team, Phys. Rev. Lett. 90, 155002 (2003).
24. W. M. Stacey and R. J. Groebner, Phys. Plasmas 16, 102504 (2009).
25. W. M. Stacey, Phys. Plasmas 17,052506 (2010). *Calc n profile98889 80-99*
26. T. Sunn Pedersen, R. S. Granetz, A. E. Hubbard, I. H. Hutchinson, E. S. Marmar, J. E. Rice, J. Terry, Nuclear Fusion **40**, 1795 (2000).
27. T. Putterich, R. Dux, E. Wolfrum, E. Viezzer and the ASDEX Upgrade Team , *36th EPS Conference on Plasma Phys. Sofia, June 29 - July 3, 2009 ECA Vol.**33E**, P-1.158 (2009)*
28. A Kallenbach, Y Andrew, M Beurskens, G Corrigan, T Eich , S Jachmich, M Kempenaars, A Korotkov, A Loarte, G Matthews , P Monier-Garbet, G Saibene , J Spence, W Suttrop and JET EFDA Contributors, Plasma Phys. Control. Fusion **46,** 431 (2004).
29. W. M. Stacey and R. J. Groebner, Phys. Plasmas 15, 012503 (2008).
30. W. M. Stacey and R. J. Groebner, Phys. Plasmas 14, 122504 (2007).
31. K. H. Burrell, et al., Rev. Sci. Instr. **75**, 3455 (2004).
32. R. J. Groebner et al, Nucl. Fusion **49** 045013 (2009)
33. W. M. Stacey, Contrib. Plasma Phys. 48, 94 (2008).
34. W. M. Stacey, Phys. Plasmas 15, 012501 (2008).
35. W. M. Stacey, Phys. Plasmas 5, 1015(1998) and 8, 3673 (2001); Nucl. Fusion 40, 965 (2000).
36. H. St. John, et al, Proc. 15th Int. Conf. on Plasma Physics and Controlled Nuclear Physics Research (Seville, Spain) vol 3 (Vienna: IAEA) p 603 (1994).

LIST OF FIGURE TITLES

Figure 1 Fit of experimental electron density measured by Thomson scattering.

Figure 2 Fit of experimental electron temperature measured by Thomson scattering.

Figure 3 Fit of experimental ion temperature measured by CER.

Figure 4 Fit of experimental carbon toroidal rotation velocity measured by CER.

Figure 5 Fit of experimental carbon poloidal rotation velocity measured by CER. (The sign convention is for a right hand system with respect to the current; i.e. the positive direction is down at the outboard midplane.)

Figure 6 Fit of radial electric field constructed from experimental measurements of carbon rotation velocities and pressure gradient.

Figure 7 Radial ion particle flux calculated from Eq. (1) using experimental data.

Figure 8 Deuterium toroidal angular momentum transfer frequency calculated from Eq. (12) using experimental data.

Figure 9 Poloidal rotation velocities for time bin 40-60% calculated in various ways from Eq. (4) for carbon and deuterium, and measured for carbon. (V_C^{calc} and V_D^{calc1} are the solutions to Eqs. (4) for D and C, and V_D^{calc2} is the solution of Eq. (4) for D with $V_C = V_C^{\exp}$. V_D^{cor} is the solution of Eq. (4) for D corrected by the difference $V_C^{calc} - V_C^{\exp}$. Note that the two calculated deuterium velocity plots and symbols fall on top of each other.)

Figure 10 Corrected deuterium poloidal rotation velocities used to calculate V_{rD}^{pinch}.

Figure 11 Deuterium pinch velocity inferred by evaluating Eq. (8) using experimental data and V_D^{av} from Fig. 10.

Figure 12 Deuterium ion particle diffusion coefficient evaluated from Eq. (10) using experimental data and momentum transfer frequency from Fig. 8.

Figure 13 Total electron and ion heat fluxes calculated from Eqs. (5) and (6) using experimental data.

Figure 14 Electron thermal diffusivity inferred from Eq. (15) using experimental data and calculated heat and particle fluxes from Figs. 12 and 7.

Figure 15 Ion thermal diffusivity inferred from Eq. (15) using experimental data and calculated heat and ion particle fluxes from Figs. 12 and 7.

Figure 16 Comparison of electron density calculated from Eq. (16) against the experimental electron density measured with Thomson scattering.

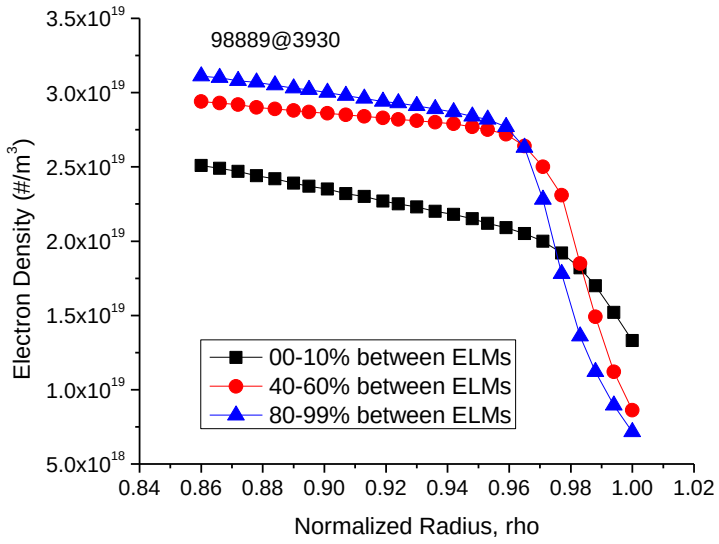
98889@3930
Electron Density (#/m3)
3.5x1019
3.0x1019
2.5x1019
2.0x1019
1.5x1019
1.0x1019
5.0x1018
0.84 0.86 0.88 0.90 0.92 0.94 0.96 0.98 1.00 1.02
Normalized Radius, rho
00-10% between ELMs
40-60% between ELMs
80-99% between ELMs

1

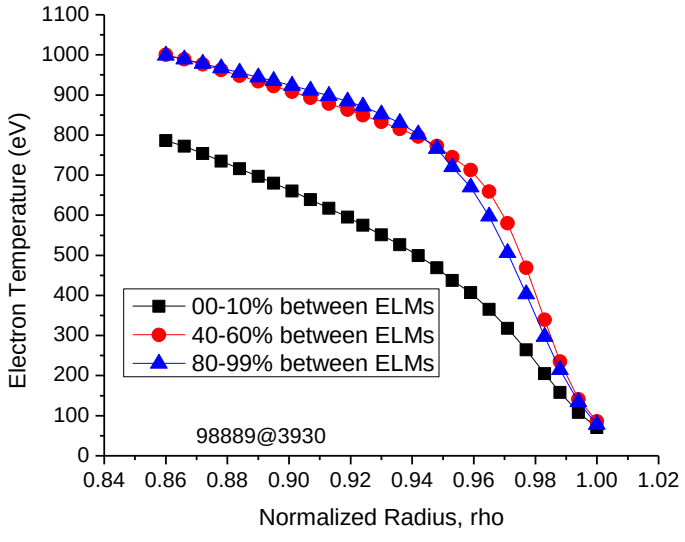
Electron Temperature (eV)
1100
1000
900
800
700
600
500
400
300
200
100
0
0.84 0.86 0.88 0.90 0.92 0.94 0.96 0.98 1.00 1.02
Normalized Radius, rho
00-10% between ELMs
40-60% between ELMs
80-99% between ELMs
98889@3930

2

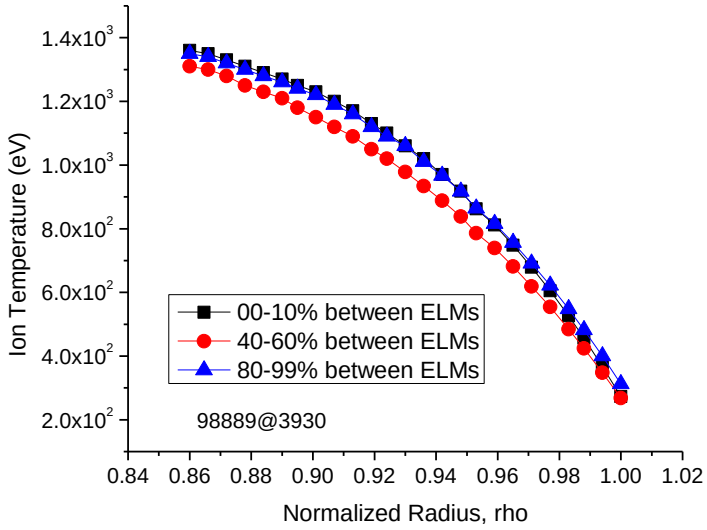
Ion Temperature (eV)
1.4x10^3
1.2x10^3
1.0x10^3
8.0x10^2
6.0x10^2
4.0x10^2
2.0x10^2
00-10% between ELMs
40-60% between ELMs
80-99% between ELMs
98889@3930
0.84 0.86 0.88 0.90 0.92 0.94 0.96 0.98 1.00 1.02
Normalized Radius, rho

3

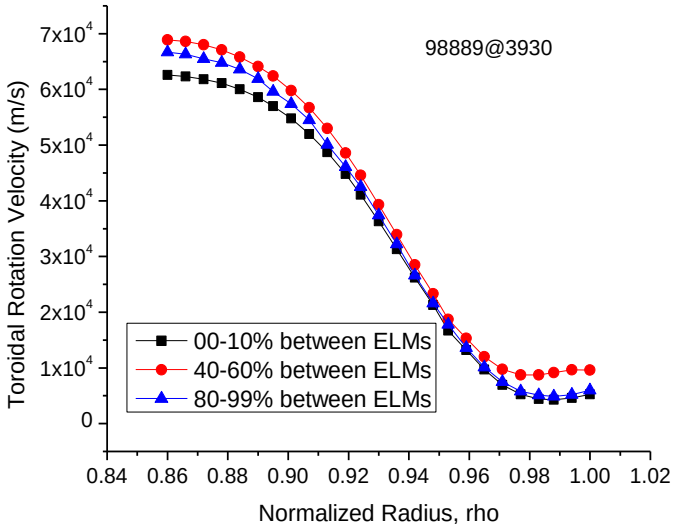
Toroidal Rotation Velocity (m/s)
7x10^4
6x10^4
5x10^4
4x10^4
3x10^4
2x10^4
1x10^4
0
98889@3930
00-10% between ELMs
40-60% between ELMs
80-99% between ELMs
0.84 0.86 0.88 0.90 0.92 0.94 0.96 0.98 1.00 1.02
Normalized Radius, rho

4

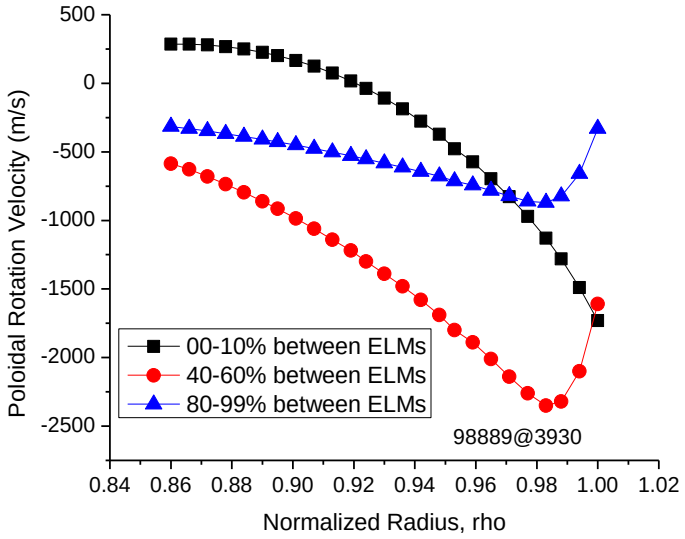
Poloidal Rotation Velocity (m/s)
500
0
-500
-1000
-1500
-2000
-2500
0.84
0.86
0.88
0.90
0.92
0.94
0.96
0.98
1.00
1.02
Normalized Radius, rho
00-10% between ELMs
40-60% between ELMs
80-99% between ELMs
98889@3930

5

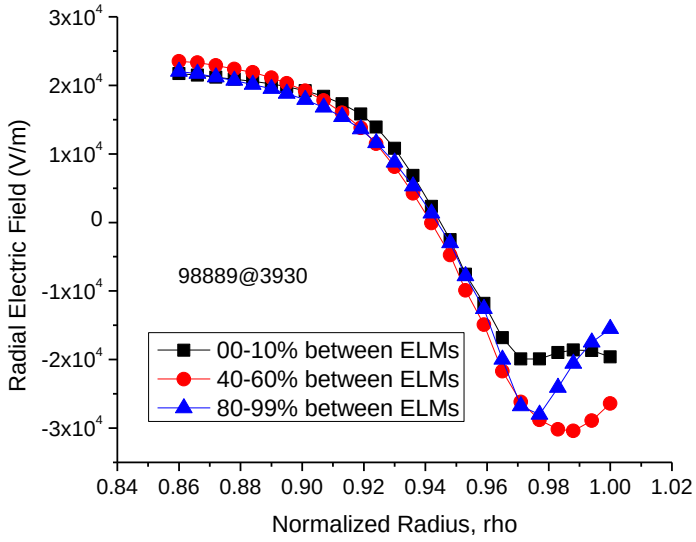
Radial Electric Field (V/m)
3x10^4
2x10^4
1x10^4
0
-1x10^4
-2x10^4
-3x10^4
0.84
0.86
0.88
0.90
0.92
0.94
0.96
0.98
1.00
1.02
Normalized Radius, rho
98889@3930
00-10% between ELMs
40-60% between ELMs
80-99% between ELMs

6

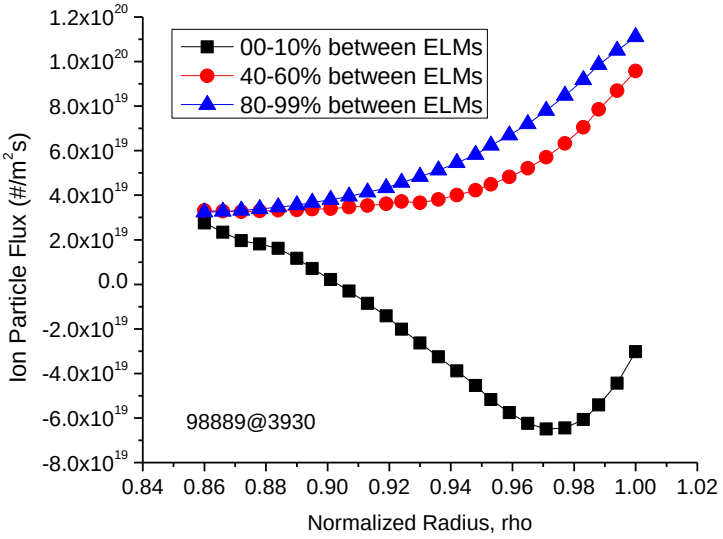
1.2x10^20
1.0x10^20
8.0x10^19
6.0x10^19
4.0x10^19
2.0x10^19
0.0
-2.0x10^19
-4.0x10^19
-6.0x10^19
-8.0x10^19
Ion Particle Flux (#/m^2s)
00-10% between ELMs
40-60% between ELMs
80-99% between ELMs
98889@3930
0.84 0.86 0.88 0.90 0.92 0.94 0.96 0.98 1.00 1.02
Normalized Radius, rho

7

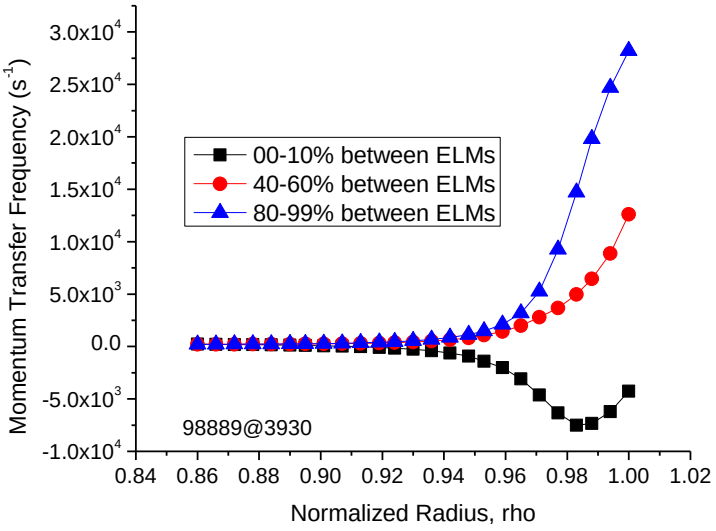
3.0x10^4
2.5x10^4
2.0x10^4
1.5x10^4
1.0x10^4
5.0x10^3
0.0
-5.0x10^3
-1.0x10^4
Momentum Transfer Frequency (s^-1)
00-10% between ELMs
40-60% between ELMs
80-99% between ELMs
98889@3930
0.84 0.86 0.88 0.90 0.92 0.94 0.96 0.98 1.00 1.02
Normalized Radius, rho

8

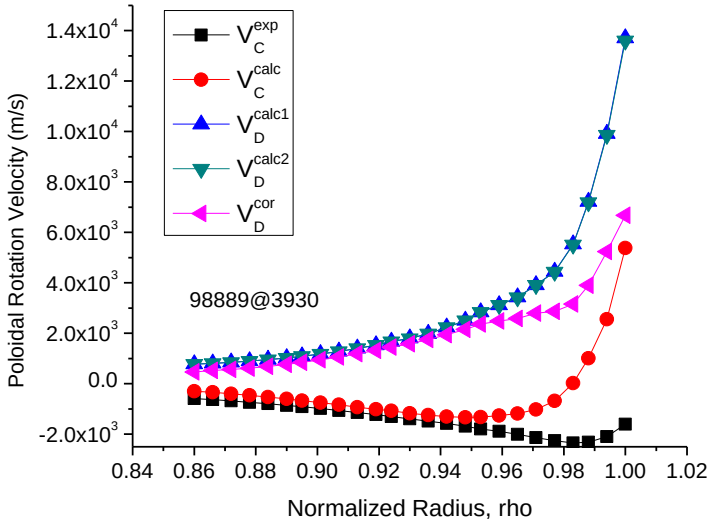
Poloidal Rotation Velocity (m/s)
1.4x10^4
1.2x10^4
1.0x10^4
8.0x10^3
6.0x10^3
4.0x10^3
2.0x10^3
0.0
-2.0x10^3
0.84 0.86 0.88 0.90 0.92 0.94 0.96 0.98 1.00 1.02
Normalized Radius, rho
V_C^exp
V_C^calc
V_D^calc1
V_D^calc2
V_D^cor
98889@3930

9

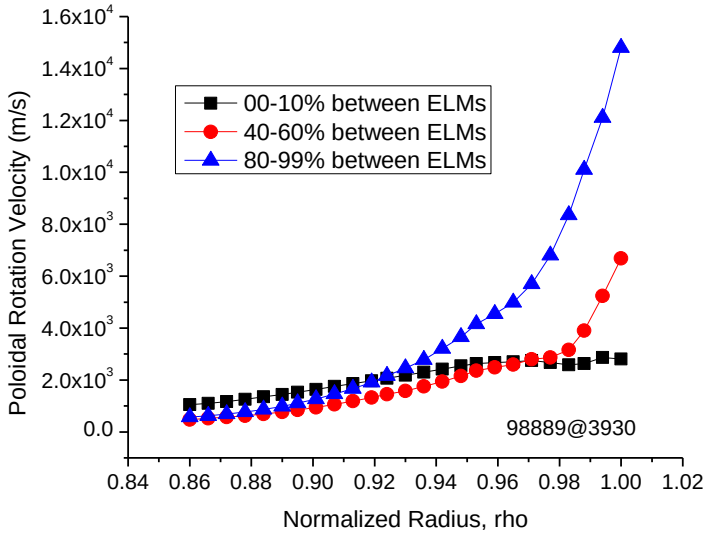
Poloidal Rotation Velocity (m/s)
1.6x10^4
1.4x10^4
1.2x10^4
1.0x10^4
8.0x10^3
6.0x10^3
4.0x10^3
2.0x10^3
0.0
0.84 0.86 0.88 0.90 0.92 0.94 0.96 0.98 1.00 1.02
Normalized Radius, rho
00-10% between ELMs
40-60% between ELMs
80-99% between ELMs
98889@3930

10

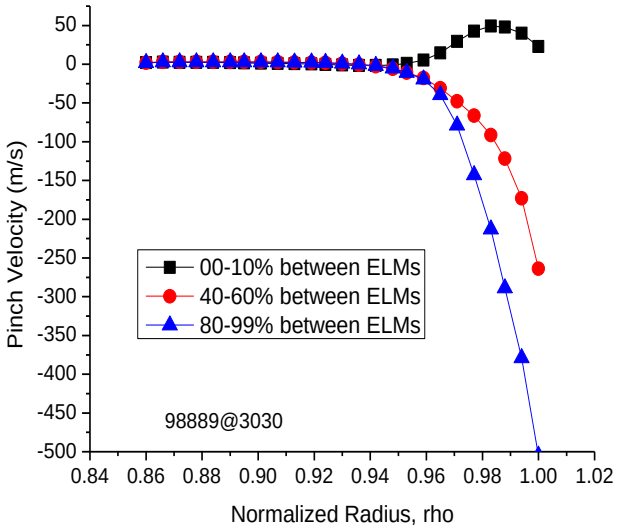
Pinch Velocity (m/s)
Normalized Radius, rho
00-10% between ELMs
40-60% between ELMs
80-99% between ELMs
98889@3030

11

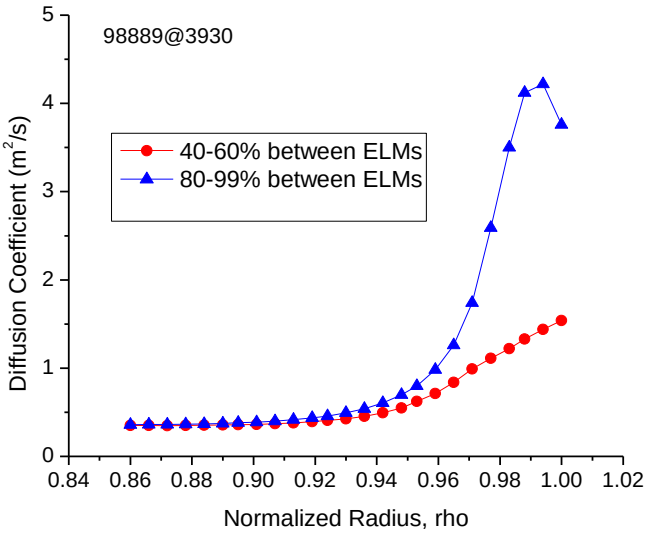
Diffusion Coefficient (m²/s)
Normalized Radius, rho
98889@3930
40-60% between ELMs
80-99% between ELMs

12

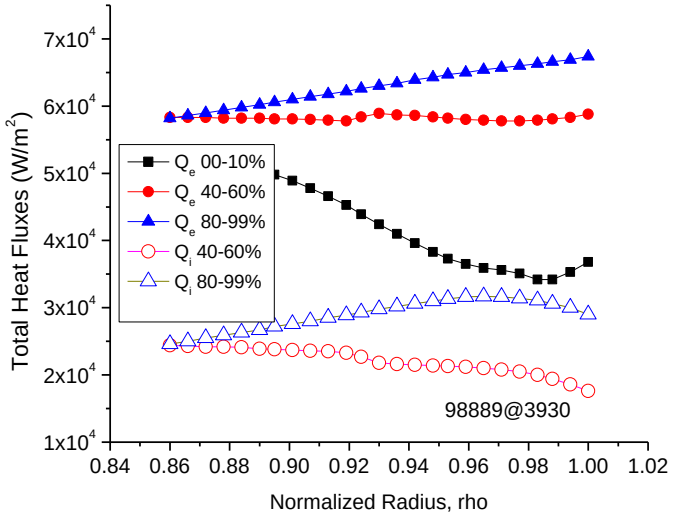
Total Heat Fluxes (W/m^2)
Normalized Radius, rho
Q_e 00-10%
Q_e 40-60%
Q_e 80-99%
Q_i 40-60%
Q_i 80-99%
98889@3930

13

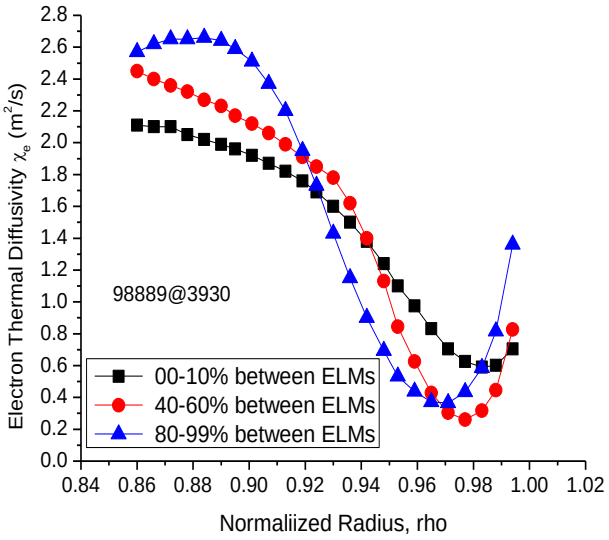
Electron Thermal Diffusivity χ_e (m^2/s)
Normaliized Radius, rho
98889@3930
00-10% between ELMs
40-60% between ELMs
80-99% between ELMs

14

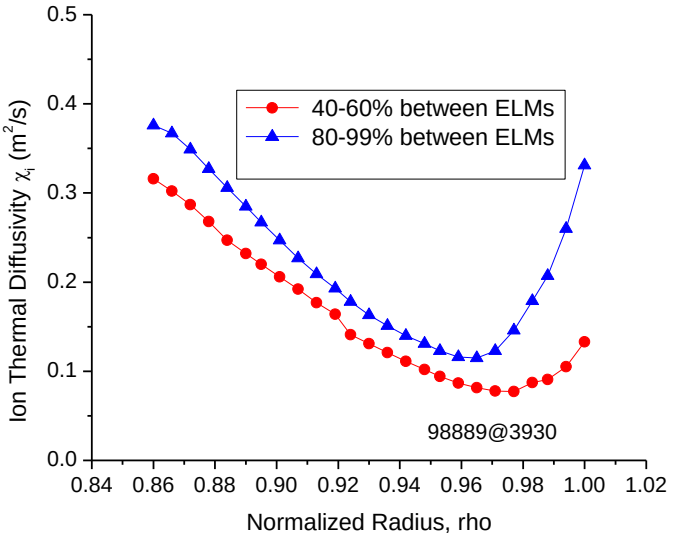
40-60% between ELMs
80-99% between ELMs
98889@3930
Ion Thermal Diffusivity χ_i (m^2/s)
Normalized Radius, rho
0.0
0.1
0.2
0.3
0.4
0.5
0.84
0.86
0.88
0.90
0.92
0.94
0.96
0.98
1.00
1.02

15

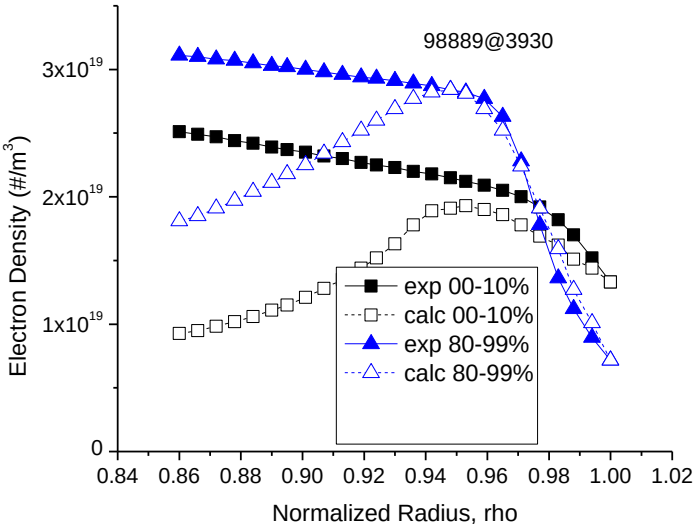
98889@3930
exp 00-10%
calc 00-10%
exp 80-99%
calc 80-99%
Electron Density (#/m^3)
Normalized Radius, rho
0
1x10^{19}
2x10^{19}
3x10^{19}
0.84
0.86
0.88
0.90
0.92
0.94
0.96
0.98
1.00
1.02

16